

The Role of Quenched Variability in Enhancing Memory Storage in Neuronal Networks

Antonio Franca
antoniofrancaib@gmail.com
June, 2024

Abstract

Recurrent network models with a behavioral time-scale plasticity rule (BTSP) can encode numerous spatial maps. Memory recall in these networks corresponds to the recovery of a bump attractor within a specific environment. This process relies on the amplitude of the spatial modulation (the first spatial Fourier mode) in the connectivity, which reflects the environment's topology. This amplitude is large for recently stored environments but diminishes for older memories due to overwriting. The network's storage capacity is defined as the most remote memory for which the first spatial Fourier mode's amplitude can still trigger a Turing instability. Interestingly, interference between stored memories manifests as a quenched variability term in the connectivity, which drives the Turing bifurcation to lower amplitudes of the first spatial Fourier mode, thereby enhancing the network's memory capacity. However, this quenched variability also leads to the formation of shifted locations for the Turing pattern, which might be undesirable for an unbiased spatial representation. We explore this trade-off between enhanced memory capacity and memory bias using analytical and numerical methods.

Contents

1	Introduction	3
2	Mathematical Modeling and Analysis	4
2.1	Analytical Steady-State Solutions	4
2.2	Deterministic Model: Analysis Without Quenched Variability	6
2.3	Fourier Series and Statistics	7
2.4	Stochastic Model: Impact of Quenched Variability	10
3	Numerical Simulations and Experiments	12
3.1	Computational Simulation of the Neural Field Model	12
3.2	Evaluation of Uniform Stability	13
3.3	Analysis of Fourier Statistics	14
3.4	Assessment of Spatial Stability	15
3.5	On Hotspots	18
4	Conclusion	18
A	Derivation of the Statistical Coefficients	19
B	Derivation of the Distribution of R_j and ψ_j	21
C	Derivation of Amplitude R and Phase Shift δ	22
D	Supplementary Code	23

1 Introduction

Understanding the mechanisms underlying memory storage and recall in the brain is a fundamental question in neuroscience. Episodic memories, which are tied to specific events and contexts, can form after a single exposure to new stimuli. A pivotal discovery in this field is the Behavioral Time-Scale Plasticity (BTSP), a form of synaptic plasticity that facilitates one-shot learning. BTSP has been observed in place cells within the hippocampal CA1 region [1, 2], where synaptic weights are adjusted following a single traversal of an environment.

BTSP allows place cells to form or shift their place fields rapidly, typically after a single event marked by a dendritic plateau potential (PP) in the postsynaptic cell. This rapid adjustment challenges traditional Hebbian learning models, which rely on repeated pre- and postsynaptic pairings. Experimental evidence suggests that BTSP enables synaptic potentiation and depression based on the temporal overlap of pre- and postsynaptic activities, mediated by eligibility traces and instructive signals.

In modeling BTSP, Milstein et al. [1] developed a biophysical network model that incorporates the plasticity rule induced by BTSP to describe synaptic updates. This network model demonstrates that BTSP can rapidly reshape population activity in response to behavioral and environmental cues. In particular, they modeled BTSP by considering a CA1 place cell receiving inputs from N excitatory CA3 place cells uniformly distributed on a circular track of length L .

It was assumed that a rat traverses a virtual linear track at a constant velocity v , a line of length L , where it is shown different simulated environments. When the rat reaches the end of the line, the end of the environment, it is teleported back to the beginning of the environment. As the rat crossed a given location denoted by x_{PP} , a plateau potential (PP) occurred either naturally (see [2]) or was artificially induced through intracellular current injection. This PP is the phenomenon responsible for BTSP plasticity updates, facilitating one-shot learning of the virtual environments.

The synaptic update rule from the biophysical model was successfully reduced to a 1D map by Roxin and Lin [3], enabling analytical study of the connectivity and the network dynamics. Furthermore, this 1D map was extended to recurrent networks, unlike the feedforward setup from Milstein et al., aiming to understand how BTSP may influence the CA3 region of the hippocampus, particularly in the context of studying memory formation. This resulting 1D map update rule accounts for the influences of both potentiation and depression and is expressed as

$$w_{ij}^n = w_{ij}^{n-1} + (P \cdot (1 - w_{ij}^{n-1}) f_P(\Delta\theta_{ij}^n) - D \cdot w_{ij}^{n-1} \cdot f_D(\Delta\theta_{ij}^n)) S_i^n S_j^n, \quad (1)$$

where $f_P(\theta)$ and $f_D(\theta)$ denote the plasticity functions for potentiation and depression, respectively, with P and D being the corresponding learning rates. Additionally, S_i^n and S_j^n are binary indicators (modeled as Bernoulli random variables) of neuronal activity in a given environment n , ensuring that synaptic weight updates occur only when both neurons i and j are active simultaneously in environment n . The term $\Delta\theta_{ij}^n$ denotes the phase difference between neuron i and neuron j . This arises from the dynamics being configured within a ring topology framework, the reasoning for which will be explained soon.

The firing rate equations of the original network model are

$$\begin{aligned} \tau \frac{d}{dt} r_1 &= -r_1 + \phi \left(\frac{1}{\kappa N} \sum_{j=1}^{MN} w_{1j} r_j S_j^k + I_0 \right) S_1^k \\ \tau \frac{d}{dt} r_2 &= -r_2 + \phi \left(\frac{1}{\kappa N} \sum_{j=1}^{MN} w_{2j} r_j S_j^k + I_0 \right) S_2^k \\ &\vdots \\ \tau \frac{d}{dt} r_i &= -r_i + \phi \left(\frac{1}{\kappa N} \sum_{j=1}^{MN} w_{ij} r_j S_j^k + I_0 \right) S_i^k \\ &\vdots \end{aligned} \quad (2)$$

where r_i is the firing rate of cell i , and ϕ is a nonlinear function. For simplicity, it is assumed that the external drive I_0 is the same for all neurons. The parameter κ sets how we scale the connectivity with respect to the size of the neuronal population encoding each position.

Despite the comprehensiveness of this network model, it can be computationally intensive due to its complexity. To address this, researchers have found that the recurrent network's topology shaped by BTSP, when incorporating sparse coding, can be approximated by a series of rings, one for each environment. Sparse coding is essential to reduce interference between memories stored in the network. In a network where every neuron encodes a place field for every environment, there would be maximal interference, making it difficult to distinguish between different memories. Sparse coding mitigates this issue by ensuring that only a fraction s of neurons are active as place cells in any given environment.

In this regime of sparse coding: (1) Interference between different memories is minimized, and (2) The interference that does occur is represented as quenched variability, which is random noise in the connectivity matrix and is uncorrelated with the environment being analyzed.

Given the sparse-coding limit (i.e., when s in $S_i^n \sim \text{Bern}(s)$ is sufficiently small), we can simplify the analysis of memory capacity in the recurrent network. Instead of dealing with the full complexity of the network, we can project the dynamics onto low-dimensional manifolds that correspond to past environments. This projection is equivalent to representing each environment with a ring model. Each ring has a connectivity profile derived analytically from the 1D map of BTSP.

$$\tau \frac{\partial r(\theta, t)}{\partial t} = -r(\theta, t) + \phi \left(\frac{1}{2\pi} \int_{-\pi}^{\pi} W(\theta - \theta') r(\theta', t) d\theta' + I_0 \right)$$

The ring model restricts the dynamics to a low-dimensional manifold that represents spatial modulations within an environment. In this approach, neurons are typically ordered according to their preferred place field in environment n .

The network connectivity itself has highly complex structure, but when projected onto the subspaces corresponding to different environments it is largely characterized by the mean correlation with that space, e.g. the amplitude of the first Fourier coefficient, and the degree of quenched variability due to interference between environments. Thus, in the ring model, the connectivity between neurons is approximated by a kernel function that encapsulates the essential features of synaptic interactions observed in the network model. The connectivity kernel is defined as

$$W(\Delta\theta) = W_0 + W_1 \cos(\Delta\theta) + \Delta W z(\Delta\theta). \quad (3)$$

Here, W_0 represents the baseline connectivity, $W_1 \cos(\Delta\theta)$ captures the spatial modulation of connectivity, and $\Delta W z(\Delta\theta)$ introduces quenched variability through a Gaussian random variable z . The amplitude of the modulation, denoted by W_1 , will be large for recently learned environments and will decrease as new environments are explored. This formulation allows the ring model to reflect the average synaptic weight and the variability introduced by BTSP. This ring model, with its simplified yet robust connectivity function, provides an analytically tractable framework to study these effects systematically.

Memory recall in neural networks can be conceptualized as the recovery of a bump attractor within a given environment. To simulate this, we start by introducing a perturbed steady state as the initial input in a ring network and observe whether a bump attractor forms. The formation of a bump attractor indicates successful memory recall. After exploring multiple environments, the storage capacity of the network is defined as the most remote memory for which the amplitude of the first spatial Fourier mode, the spatial modulation of a given environment W_1 , can still elicit a Turing instability.

To examine memory capacity, we will then analyze the range of spatial modulation values, W_1 , that enable the ring network to produce a bump. With the necessary background and motivation for studying this topic established, we can proceed to the core of this thesis: investigating how introducing variability in neuronal connectivity affects memory storage capacity in recurrent networks with BTSP plasticity.

2 Mathematical Modeling and Analysis

2.1 Analytical Steady-State Solutions

Consider the ring model described by the equation

$$\tau \frac{\partial r(\theta, t)}{\partial t} = -r(\theta, t) + \phi \left(\frac{1}{2\pi} \int_{-\pi}^{\pi} W(\theta - \theta') r(\theta', t) d\theta' + I_0 \right), \quad (4)$$

where the connectivity kernel is given by $W(\Delta\theta) = W_0 + W_1 \cos(\Delta\theta) + \Delta W z(\Delta\theta)$.

Here, W_0 is the homogeneous synaptic connectivity, W_1 represents the spatially modulated connectivity, $\Delta W(\Delta\theta)$ represents the quenched variability, modeled as a white noise process that introduces random fluctuations in synaptic connectivity. The parameter I_0 is the external input to the system, and ϕ is a nonlinear function characterizing the response of the neurons. Finally, τ represents the time constant of the neural system, often assumed to be 1 for simplicity in calculations.

The quenched variability is introduced as a Gaussian noise process,

$$\Delta W(\theta) = \sqrt{V(\theta)}z, \quad z \sim N(0, 1)$$

where $V(\theta)$ is the variance of the memory trace. For context, this variance of the memory trace refers roughly to how much the neural connections can vary when storing a particular memory. This variance is modeled as

$$V(\theta) = A + B \cos(\theta) + C \cos^2(\theta)$$

With quenched variability, each neuron features a distinct connectivity kernel, thereby disrupting spatial symmetries in the ring's activity. In Figure 1, we plot the connectivity kernels of each neuron, versus the connectivity without variability (which is identical for all the neurons).

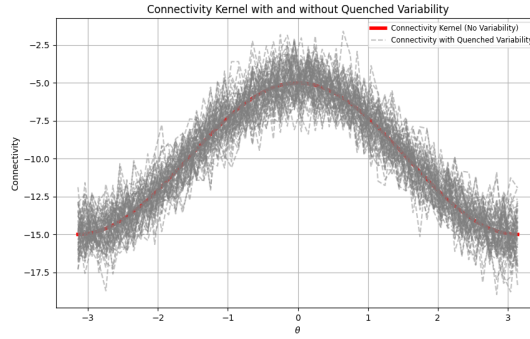


Figure 1: Effect of quenched variability on neuronal connectivity kernels.

We start the analysis by considering the homogeneous steady states.

In the steady-state analysis, the influence of the spatial component W_1 vanishes because the cosine term integrates to zero over a full period. Furthermore, given that $\Delta W(\theta)$ is defined as $\sqrt{V(\theta)}z$, the quenched variability is negated by the zero-mean characteristic of z , assuming its behavior is independent across θ . Consequently, the steady-state equation simplifies to

$$r_0 = \phi \left(\frac{r_0}{2\pi} \int_{-\pi}^{\pi} W_0 + W_1 \cos(\theta') + \Delta W(\theta') d\theta' + I_0 \right) = \phi(r_0 W_0 + I_0). \quad (5)$$

Here, r_0 represents the activity of the homogeneous steady state. The stationary solutions for the steady-state firing rate r_0 are determined by the equation given in (5). In our study, we define the nonlinearity ϕ using the following piecewise function

$$\phi(x) = \begin{cases} x^2 & \text{for } 0 \leq x \leq 1, \\ 2\sqrt{x - \frac{3}{4}} & \text{for } x > 1, \\ 0 & \text{otherwise.} \end{cases}$$

Depending on the value of the input I_0 and the coupling W_0 , the steady-state solutions are then given as follows

- For the range $0 \leq r_0 W_0 + I_0 \leq 1$

$$r_0 = \frac{1 - 2W_0 I_0 \pm \sqrt{1 - 4W_0 I_0}}{2W_0^2}.$$

- For the case where $r_0 W_0 + I_0 > 1$

$$r_0 = 2W_0 \pm 2\sqrt{W_0^2 + I_0 - \frac{3}{4}}.$$

We could have chosen to analytically determine the bounds of these solutions. However, as this task is non-trivial and not the central focus of this thesis, we opted to hardcode masks (see the function code in Appendix D) in the code to directly compute the solutions.

In Figure 2, we observe the solutions for different W_0 and I_0 parameter values. The key insight for subsequent coding is that with W_0 negative, only one steady-state solution exists, denoted as r_{02} in the code. Figure 2 presents only two scenarios; readers are encouraged to explore other solutions by adjusting the parameters themselves. This can be done by using the Jupyter notebooks in [this link](#). Once the stationary solutions are identified, we advance to a more intriguing aspect of the study: the linear stability analysis of these solutions.

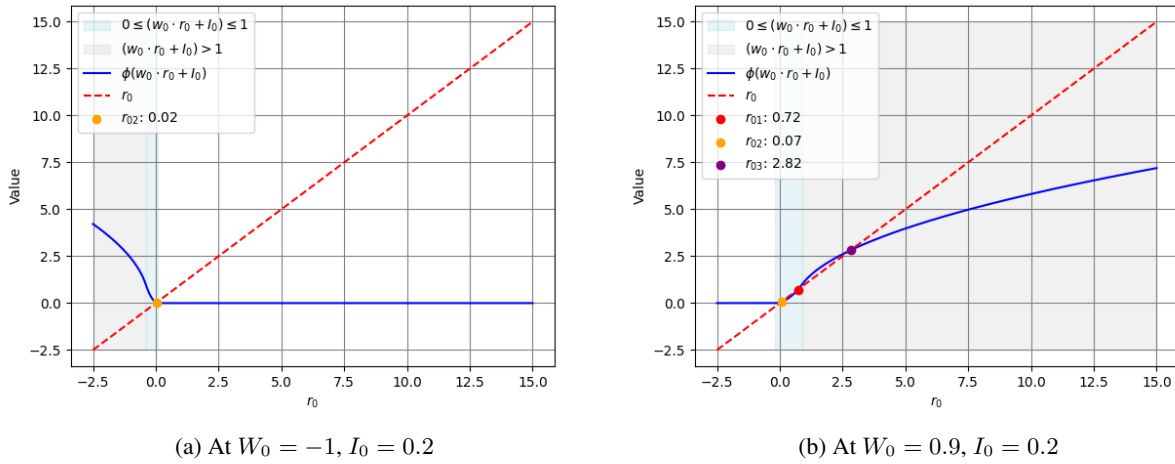


Figure 2: Steady-State Solutions for different W_0 and I_0 parameter values.

2.2 Deterministic Model: Analysis Without Quenched Variability

The process of linear stability analysis involves evaluating the stability of a steady state by analyzing the response of the system to small perturbations. In this context, we first analyze the deterministic case of the ring model described by equation (4). Subsequently, we explore the stochastic scenario, incorporating variability, with the primary objective of examining the differences in memory storage capacity. In the deterministic scenario, the model excludes the quenched variability from the connectivity, providing a simplified framework to understand the baseline dynamics of the system.

Next, we consider small perturbations around these steady states

$$r(\theta, t) = r_0 + \delta r_0 e^{\lambda_0 t} + \delta r_1 \cos(\theta) e^{\lambda_1 t} \quad (6)$$

This perturbation includes a uniform part $\delta r_0 e^{\lambda_0 t}$ and a spatially modulated part $\delta r_1 \cos(\theta) e^{\lambda_1 t}$, where δr_0 and δr_1 are small amplitudes of perturbation, and λ_0 and λ_1 are the growth rates of these perturbations.

By integrating over the population, we observe

$$\frac{1}{2\pi} \int_{-\pi}^{\pi} (W_0 + W_1 \cos(\theta - \theta')) (r_0 + \delta r_0 e^{\lambda_0 t} + \delta r_1 \cos(\theta') e^{\lambda_1 t}) d\theta' = W_0 r_0 + W_0 \delta r_0 e^{\lambda_0 t} + \frac{W_1}{2} \delta r_1 \cos(\theta) e^{\lambda_1 t}. \quad (7)$$

We then plug the perturbation 6 into the ring model equation, assuming $\tau = 1$ for simplicity. By linearizing the nonlinearity ϕ around $W_0 r_0 + I_0$, we obtain the following expression for the time evolution of the perturbations

$$\begin{aligned} \lambda_0 \delta r_0 e^{\lambda_0 t} + \lambda_1 \delta r_1 \cos(\theta) e^{\lambda_1 t} = & - (r_0 + \delta r_0 e^{\lambda_0 t} + \delta r_1 \cos(\theta) e^{\lambda_1 t}) \\ & + \phi(r_0 W_0 + I_0) + \phi'(r_0 W_0 + I_0) \left(W_0 \delta r_0 e^{\lambda_0 t} + \frac{W_1 \delta r_1 \cos(\theta) e^{\lambda_1 t}}{2} \right). \end{aligned}$$

By equating the terms corresponding to λ_0 and λ_1 to each other, and utilizing the condition $-r_0 + \phi(r_0 W_0 + I_0) = 0$, we can solve for the growth rates

$$\lambda_0 = -1 + \phi'_0 W_0,$$

and

$$\lambda_1 = -1 + \phi'_0 \frac{W_1}{2},$$

where ϕ'_0 is the slope of the transfer function evaluated at the steady state.

To ensure the stability of the steady state and to avoid uniform instability, the homogeneous synaptic connectivity W_0 must satisfy

$$W_0 < \frac{1}{\phi'_0}.$$

Finally, we determine the critical value of the spatially modulated connectivity W_1 , denoted as W_1^{cr} , beyond which the steady state becomes unstable to spatial perturbations

$$W_1^{cr} = \frac{2}{\phi'_0}.$$

We numerically validate these theoretical results in Section 3.2, and Section 3.4.

2.3 Fourier Series and Statistics

Having analyzed the deterministic case of the ring model, we now turn to the main focus of this thesis: exploring the role of quenched variability in enhancing memory storage within neuronal networks.

Consider the stochastic variant of the ring model, where the connectivity kernel function is now given by

$$W(\Delta\theta) = W_0 + W_1 \cos(\Delta\theta) + \Delta W(\Delta\theta).$$

Recall that W_0 represents the homogeneous synaptic connectivity, W_1 signifies spatially modulated connectivity, and $\Delta W(\theta)$ denotes the quenched variability in connectivity.

The quenched variability in the model is introduced as a Gaussian noise process, defined by

$$\Delta W(\theta) = \sqrt{V(\theta)} z,$$

where z is a zero-mean Gaussian random variable with unit variance, and $V(\theta)$, the variance of the memory trace, is expressed as

$$V(\theta) = A + B \cos(\theta) + C \cos^2(\theta) = A + \frac{C}{2} + B \cos(\theta) + \frac{C}{2} \cos(2\theta). \quad (8)$$

Expressing $\Delta W(\theta)$ in terms of its Fourier series, we note that since $\Delta W(\theta)$ is real-valued, the complex coefficients of the Fourier series satisfy $c_{-j} = \overline{c_j}$, and $c_0 = 0$ due to z being zero-mean. The Fourier series of $\Delta W(\theta)$ is

$$\begin{aligned} \Delta W(\theta) &= \sum_{j=-\infty}^{\infty} c_j e^{ij\theta} = c_0 + \sum_{j=1}^{\infty} (c_j e^{ij\theta} + c_{-j} e^{-ij\theta}) \\ &= \sum_{j=1}^{\infty} (\alpha_j - i\beta_j)(\cos(j\theta) + i\sin(j\theta)) + (\alpha_j + i\beta_j)(\cos(j\theta) - i\sin(j\theta)), \end{aligned}$$

which simplifies to the real Fourier series of $\Delta W(\theta)$

$$\Delta W(\theta) = 2 \sum_{j=1}^N \alpha_j \cos(j\theta) + \beta_j \sin(j\theta), \quad (9)$$

where we truncate the series at N (neuron populations) since higher harmonics would correspond to spatial frequencies not supported by the discrete nature of the neuron populations. I made an insightful simulation to illustrate this concept in a Jupyter notebook, which is available in the [GitHub repository](#) for this thesis.

Because the variability is a zero-mean Gaussian process, the coefficients α_j and β_j are also zero-mean Gaussian random variables whose variances and covariances must be determined self-consistently. We do this through appropriate averaging. Specifically, we calculate

$$V(\theta) = \langle \Delta W(\theta)^2 \rangle = 4 \left\langle \left(\sum_{j=1}^N \alpha_j \cos(j\theta) + \beta_j \sin(j\theta) \right) \left(\sum_{l=1}^N \alpha_l \cos(l\theta) + \beta_l \sin(l\theta) \right) \right\rangle.$$

Expanding this and assuming independence between α_j and β_j (hence $\langle \alpha_j \beta_l \rangle = 0$), we find

$$V(\theta) = 4 \sum_{j=1}^N \sum_{l=1}^N (\langle \alpha_j \alpha_l \rangle \cos(j\theta) \cos(l\theta) + \langle \beta_j \beta_l \rangle \sin(j\theta) \sin(l\theta)),$$

where the covariances $\langle \alpha_j \beta_l \rangle$ cancel out.

$$V(\theta) = 4 \sum_{j=1}^N \sum_{l=1}^N (\langle \alpha_j \alpha_l \rangle \cos(j\theta) \cos(l\theta) + \langle \alpha_j \beta_l \rangle \cos(j\theta) \sin(l\theta) + \langle \beta_j \alpha_l \rangle \sin(j\theta) \cos(l\theta) + \langle \beta_j \beta_l \rangle \sin(j\theta) \sin(l\theta))$$

Utilizing trigonometric identities, $V(\theta)$ simplifies to

$$V(\theta) = 2 \sum_{j=1}^N \sum_{l=1}^N (\langle \alpha_j \alpha_l \rangle + \langle \beta_j \beta_l \rangle) \cos((j-l)\theta) + 2 \sum_{j=1}^N \sum_{l=1}^N (\langle \alpha_j \alpha_l \rangle - \langle \beta_j \beta_l \rangle) \cos((j+l)\theta) \quad (10)$$

We can determine some of the coefficients in Equation-10 by employing the expressions for $V(\theta)$ given in Equations 8 and 10, supplemented with additional analytical methods. For detailed calculations, please refer to Appendix A.

The analytical solutions resulting in coefficients of interest are summarized as follows

$$\begin{aligned} \langle \alpha_1^2 \rangle &= \frac{1}{2N} \left(A + \frac{3C}{4} \right), \\ \langle \beta_1^2 \rangle &= \frac{1}{2N} \left(A + \frac{C}{4} \right), \\ \langle \alpha_j^2 \rangle &= \langle \beta_j^2 \rangle = \frac{1}{2N} \left(A + \frac{C}{2} \right) \quad \text{for } j \neq 1, \\ \langle \alpha_j \alpha_{j+1} \rangle &= \langle \beta_j \beta_{j+1} \rangle = \frac{B}{4N}, \\ \langle \alpha_j \alpha_{j+2} \rangle &= \langle \beta_j \beta_{j+2} \rangle = \frac{C}{8N}. \end{aligned}$$

A comparison of these theoretical findings with numerical simulations of a quenched Gaussian white-noise process are presented in Section-3.3.

With this knowledge in hand, we can compute the amplitudes and phases of the different modes in the Fourier series representation of the quenched variability in the connectivity kernel. We have

$$W(\theta) = W_0 + W_1 \cos(\theta) + \Delta W(\theta) = W_0 + W_1 \cos(\theta) + 2 \sum_{j=1}^N \alpha_j \cos(j\theta) + \beta_j \sin(j\theta),$$

which can be re-expressed as

$$W(\theta) = W_0 + W_1 \cos(\theta) + \sum_{j=1}^N R_j \cos(j\theta + \psi_j),$$

where R_j and ψ_j are the amplitude and phase of the modes, respectively. These are derived from the Fourier coefficients α_j and β_j , with

$$R_j = 2\sqrt{\alpha_j^2 + \beta_j^2},$$

$$\psi_j = \arctan \left(\frac{\beta_j}{\alpha_j} \right).$$

Given that α_j and β_j are zero-mean Gaussian variables with the specified variances and covariances, we can denote their complete distributions using a multivariate normal distribution. For simplicity, let's consider a vector \mathbf{X} that contains all α_j and β_j

$$\mathbf{X}^T = (\alpha_1 \quad \alpha_2 \quad \cdots \quad \alpha_N \quad \beta_1 \quad \beta_2 \quad \cdots \quad \beta_N).$$

Since α_j and β_j are zero-mean, the mean vector μ is $\mu = \mathbf{0}$. The covariance matrix Σ for \mathbf{X} can be constructed as follows

$$\Sigma = \begin{pmatrix} \Sigma_\alpha & \mathbf{0} \\ \mathbf{0} & \Sigma_\beta \end{pmatrix}$$

where Σ_α and Σ_β are the covariance matrices for α_j and β_j respectively. Given the variances and covariances, these matrices will have the following form. For Σ_α

$$\Sigma_\alpha = \frac{1}{2N} \begin{pmatrix} A + \frac{3C}{4} & \frac{B}{2} & \frac{C}{4} & \# & \cdots & \# \\ \frac{B}{2} & A + \frac{C}{2} & \frac{B}{2} & \frac{C}{4} & \cdots & \# \\ \frac{C}{4} & \frac{B}{2} & A + \frac{C}{2} & \frac{B}{2} & \cdots & \# \\ \# & \frac{C}{4} & \frac{B}{2} & A + \frac{C}{2} & \cdots & \# \\ \vdots & \vdots & \vdots & \vdots & \ddots & \vdots \\ \# & \# & \# & \# & \cdots & A + \frac{C}{2} \end{pmatrix}$$

Similarly for Σ_β

$$\Sigma_\beta = \frac{1}{2N} \begin{pmatrix} A + \frac{C}{4} & \frac{B}{2} & \frac{C}{4} & \# & \cdots & \# \\ \frac{B}{2} & A + \frac{C}{2} & \frac{B}{2} & \frac{C}{4} & \cdots & \# \\ \frac{C}{4} & \frac{B}{2} & A + \frac{C}{2} & \frac{B}{2} & \cdots & \# \\ \# & \frac{C}{4} & \frac{B}{2} & A + \frac{C}{2} & \cdots & \# \\ \vdots & \vdots & \vdots & \vdots & \ddots & \vdots \\ \# & \# & \# & \# & \cdots & A + \frac{C}{2} \end{pmatrix}$$

So, the joint distribution of \mathbf{X} is given by

$$\mathbf{X} \sim \mathcal{N}(\mathbf{0}, \Sigma)$$

where Σ is the block diagonal matrix containing Σ_α and Σ_β .

With this foundational knowledge, we deduce the distributions for R_j and ψ_j . These derivations are elaborated upon in Appendix B, where we establish

$$R_j \sim \text{Rayleigh} \left(2 \cdot \sqrt{\frac{A + \frac{C}{2}}{N}} \right),$$

$$\tan(\psi_j) = \frac{\beta_j}{\alpha_j} \sim \text{Cauchy} \left(0, \frac{\sqrt{\langle \beta_j^2 \rangle}}{\sqrt{\langle \alpha_j^2 \rangle}} \right),$$

which implies that

$$\psi_j = \arctan \left(\frac{\beta_j}{\alpha_j} \right) \sim \text{Uniform} \left(-\frac{\pi}{2}, \frac{\pi}{2} \right) \quad \text{if } \langle \alpha_j^2 \rangle = \langle \beta_j^2 \rangle.$$

This last condition is satisfied for all $j \neq 1$, as previously derived, but also for $j = 1$ when $C = 0$. We verify these theoretical distributions by simulating them experimentally in Section-3.3.

2.4 Stochastic Model: Impact of Quenched Variability

The inherent randomness of the system, known as quenched variability, does not depend on the number of positions, denoted by N . However, the impact of this variability on the system's modes diminishes inversely with N , following a $1/N$ pattern. This implies that near instabilities associated with spatially modulated modes, the magnitude of N becomes crucial. Remarkably, as N approaches infinity, the system mimics a condition devoid of noise, maintaining the total power of the quenched variability intact. Conversely, when N is finite, any spatial bifurcation in the system will be shifted.

In analyzing Turing bifurcations, we can determine their impact analytically. Specifically, the connectivity pattern for a given cell i is expressed as

$$W(\theta_i - \theta_j) = W_0 + W_1 \cos(\theta_i - \theta_j) + \sqrt{V(\theta_i - \theta_j)} z(\theta_i - \theta_j).$$

It is important to recall that the variable z varies for each neuron pair (i, j) . To assess how the bifurcation shifts, we need to isolate the part of variability that aligns with the cosine mode.

The reason is that quenched variability contributes to the amplitude of modulation in this relevant mode for instability. The integral of higher harmonic terms of the form $R_j \cos(j\theta + \phi_j)$ will yield terms involving $\cos(j\theta + \phi_j)$. When these are integrated against $\cos(\theta)$ perturbation, they yield zero unless $j = 1$, given the orthogonality of cosine functions at different frequencies over a symmetric interval.

On average, the quenched variability will then contribute an amplitude $\langle R_1 \rangle$ to the connectivity. Given we know the distribution of R_j for all modes, we easily estimate

$$\langle R_1 \rangle = \sqrt{\frac{\pi}{2N} \left(A + \frac{C}{2} \right)}.$$

However the phase is also important. If $\psi = 0$ then the quenched variability will add to W_1 and make an instability more likely. However, if $\psi = \pi$ then the quenched variability will have the opposite effect and make an instability less likely. Given that there is a distinct phase ψ for each neuron in the network, if N is large enough we can expect that for some of them $\psi \sim 0$. The quenched variability therefore always makes the instability more likely, shifting the bifurcation to lower values of W_1 .

To calculate the new critical value analytically, we assume then $\psi = 0$ for simplicity, and use the expected value R_1 in the calculations. Analogously to what we did in Equation 7, we see

$$\frac{1}{2\pi} \int_{-\pi}^{\pi} \sum_{j=1}^N \langle R_j \rangle \cos(j(\theta - \theta')) (r_0 + \delta r_0 e^{\lambda_0 t} + \delta r_1 \cos(\theta') e^{\lambda_1 t}) d\theta' = \frac{\langle R_1 \rangle \delta r_1 e^{\lambda_1 t} \cos(\theta)}{2}.$$

and this holds because we can interchange the integral and the summation, as the series converges, the integration and summation are both well-defined, and the integral operator is linear.

If we then plug the perturbation, under the new connectivity kernel with variability, we obtain

$$\begin{aligned} \lambda_0 \delta r_0 e^{\lambda_0 t} + \lambda_1 \delta r_1 \cos(\theta) e^{\lambda_1 t} = & - (r_0 + \delta r_0 e^{\lambda_0 t} + \delta r_1 \cos(\theta) e^{\lambda_1 t}) \\ & + \phi(r_0 W_0 + I_0) + \phi'(r_0 W_0 + I_0) \left(W_0 \delta r_0 e^{\lambda_0 t} + \frac{W_1 \delta r_1 \cos(\theta) e^{\lambda_1 t}}{2} + \frac{\langle R_1 \rangle \delta r_1 e^{\lambda_1 t} \cos(\theta)}{2} \right), \end{aligned}$$

and this yields the same critical value for W_0 due to the coefficient c_0 being zero, and a new growth rate for λ_1

$$\lambda_1 = -1 + \frac{\phi'_0}{2} W_1 + \frac{\phi'_0}{2} \langle R_1 \rangle$$

which yields a new critical value

$$W_1^{\text{cr}} = \frac{2}{\phi'_0} - \langle R_1 \rangle.$$

This equation indicates that the Turing bifurcation, leading to a bump instability, will occur at lower values of W_1 than in the case without quenched variability. We validate these theoretical results in Section 3.4, presenting bifurcation diagrams that explore the conditions under which W_1 induces a Turing bifurcation, i.e., the formation of a bump.

For the first mode $j = 1$, associated with a bump-like feature, the amplitude is denoted by R_1 and given by:

$$R_1 = 2\sqrt{\alpha_1^2 + \beta_1^2}.$$

Since α and β are random variables, R_1 and the phase of the modulation become random variables as well. The mean amplitude $\langle R \rangle$ is then found by integrating over the distributions of α and β . [See appendix for detailed calculations:](#)

$$\langle R_1 \rangle = \sqrt{\frac{2\pi}{N} \left(A + \frac{C}{2} \right)}.$$

The new condition for the critical connectivity, taking into account the mean amplitude from the variability, is:

$$W_1^{cr} = \frac{2}{\phi_0'} - \langle R_1 \rangle.$$

Given the relevant connectivity kernel:

$$W(\theta) = W_0 + W_1 \cos(\theta) + R_1 \cos(\theta + \psi_1),$$

we express it as a single cosine term using trigonometric identities:

$$W(\theta) = W_0 + R \cos(\theta - \delta),$$

where R and δ are defined by:

$$R = \sqrt{W_1^2 + 2W_1R_1 \cos(\psi_1) + R_1^2},$$

$$\tan(\delta) = \frac{R_1 \sin(\psi_1)}{W_1 + R_1 \cos(\psi_1)}.$$

See appendix on how to derive these terms [C](#). With the introduction of R_1 and ψ_1 , the effective connectivity strength is now R , and thus, the new critical condition becomes:

$$R < \frac{2}{\phi_0'}.$$

Squaring both sides to facilitate algebraic manipulation, we derive:

$$W_1^2 + 2W_1R_1 \cos(\psi_1) + R_1^2 < \left(\frac{2}{\phi_0'} \right)^2.$$

$R_1 \cos(\psi_1)$ modulates the stability threshold, either enhancing or reducing the permissible range of W_1 depending on the sign and magnitude of $\cos(\psi_1)$, while R_1^2 always raises the threshold.

This is solved for:

$$W_{1+} = -R_1 \cos(\psi_1) + \sqrt{\left(\frac{2}{\phi_0'} \right)^2 - R_1^2 \sin^2(\psi_1)},$$

$$W_{1-} = -R_1 \cos(\psi_1) - \sqrt{\left(\frac{2}{\phi_0'} \right)^2 - R_1^2 \sin^2(\psi_1)}.$$

and the squared inequality holds for:

$$W_{1-} < W_1 < W_{1+}.$$

However, when squaring to solve the quadratic, we must remember that this introduces extra solutions. Specifically, we see that we only need $W_1 < W_{1+}$, thus the new critical

$$W_1^{cr} = -R_1 \cos(\psi_1) + \sqrt{\left(\frac{2}{\phi_0'} \right)^2 - R_1^2 \sin^2(\psi_1)},$$

[In practical and theoretical calculations, we may approximate \$\langle R_j \rangle\$ and \$\langle \phi_j \rangle\$ to model the system's behavior under stochastic influences. Thus, the expected connectivity kernel is given by:](#)

$$W(\theta) = W_0 + W_1 \cos(\theta) + \sum_{j=1}^N \langle R_j \rangle \cos(j\theta + \langle \phi_j \rangle).$$

3 Numerical Simulations and Experiments

3.1 Computational Simulation of the Neural Field Model

For the numerical analysis, we employ the Finite-Elements Collocation Method to simulate the neural field model.

The continuous ring model is described by the following integro-differential equation

$$\frac{\partial r(\theta, t)}{\partial t} = -r(\theta, t) + \phi \left(\frac{1}{2\pi} \int_{-\pi}^{\pi} W(\theta - \theta') r(\theta', t) d\theta' + I_0 \right), \quad (11)$$

where $r(\theta, t)$ represents the activity at phase θ and time t , ϕ is the nonlinear function, $W(\theta - \theta')$ is the connectivity kernel, and I_0 is the external input.

We discretize the domain using the collocation method with N nodes, corresponding to different neurons. This discretization generates collocation points $\{\theta_i \text{ such that } \theta_i = -\pi + \frac{2\pi}{N}i; \forall i \in \{1, 2, \dots, N\}\}$, evenly spaced by $\Delta\theta = \frac{2\pi}{N-1}$. At these points, the original equation holds

$$\frac{\partial r(\theta_i, t)}{\partial t} = -r(\theta_i, t) + \phi \left(\frac{1}{2\pi} \int_{-\pi}^{\pi} W(\theta_i - \theta') r(\theta', t) d\theta' + I_0 \right).$$

We approximate the integral using the composite trapezoidal rule ¹, expressed as

$$\frac{1}{2\pi} \int_{-\pi}^{\pi} W(\theta_i - \theta') r(\theta', t) d\theta' \approx \sum_{j=1}^N W(\theta_i - \theta_j) R_j(t) p_j \frac{\Delta\theta}{2\pi}, \quad (12)$$

where $R_j(t)$ represents the activity at collocation points, and p_j are integration weights, set to $\frac{1}{2}$ at endpoints and 1 otherwise. As shown in [4], this trapezoidal formula is second-order accurate with respect to $\Delta\theta$, which means that the error in the approximation decreases quadratically as the step size decreases.

The differential equation at each collocation point is then approximated by:

$$\frac{\partial R_i(t)}{\partial t} = -R_i(t) + \phi \left(\sum_{j=1}^N W(\theta_i - \theta_j) R_j(t) \frac{p_j}{N-1} + I_0 \right),$$

and expressed in matrix form as

$$\frac{d\mathbf{R}(t)}{dt} = -\mathbf{R}(t) + \phi(\mathbf{M}\mathbf{R}(t) + I_0), \quad (13)$$

where \mathbf{M} is the matrix with elements $M_{ij} = W(\theta_i, \theta_j) \cdot \frac{p_j}{N-1}$.

Finally, this system of ordinary differential equations is solved numerically using a solver such as `solve_ivp` in Python to track the temporal evolution of the network's activity.

¹The composite trapezoidal rule employs piecewise-linear interpolations at the collocation points.

3.2 Evaluation of Uniform Stability

In this section, we explore the stability conditions for homogeneous synaptic connectivity denoted by W_0 . According to our theoretical framework, for uniform stability, W_0 must satisfy the following inequality

$$W_0 < \frac{1}{\phi'(W_0)}.$$

This condition is derived and discussed extensively in Section 2.2.

To empirically validate this theoretical condition, we constructed bifurcation diagrams. These diagrams visually represent the solutions r_0 as functions of W_0 for fixed values of the external input I_0 .

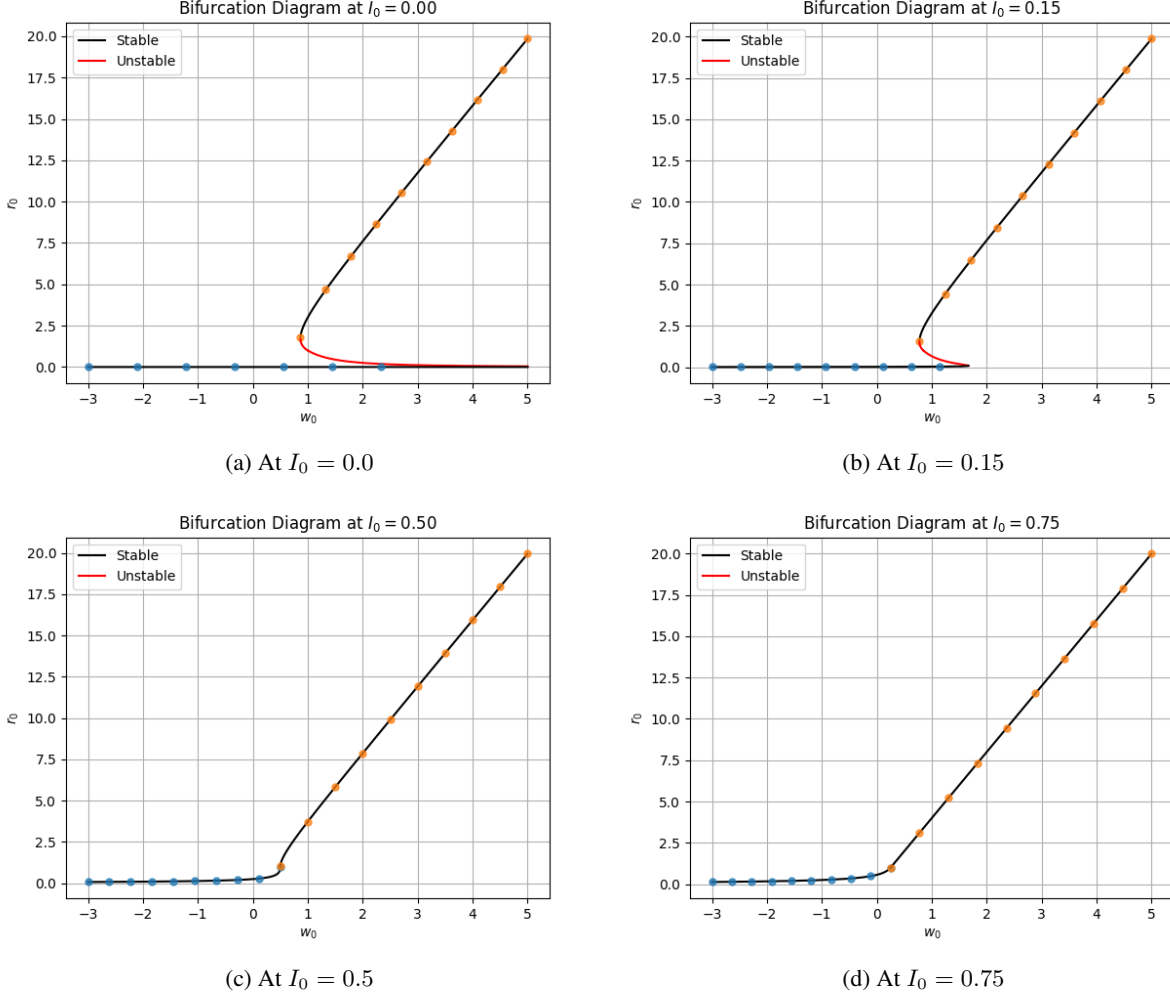


Figure 3: Bifurcation diagrams illustrating the W_0 parameter across different I_0 values.

Each diagram is color-coded to differentiate between stable and unstable solutions—red for unstable and black for stable. Our observations confirm that solutions derived from $r_{.02}$ and $r_{.03}$ are inherently stable under the parameters specified in the code.

The plotted dots represent the end points of a numerical simulation that solves the dynamic equation

$$\frac{dr_0}{dt} = -r_0 + \phi(W_0 r_0 + I_0).$$

These simulations start from theoretical solution points, and their trajectories indicate the accuracy of our theoretical predictions. Specifically, the dots that align with stable theoretical predictions remain close to their initial conditions,

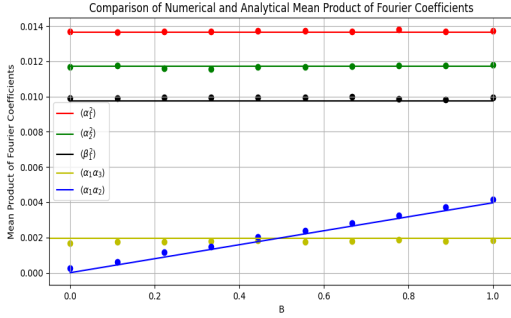
confirming the equilibrium's stability. In the case of unstable solutions, the inherent numerical instabilities caused by the finite precision of computer arithmetic can significantly alter trajectories, causing some of them to diverge from their theoretical paths. This divergence has been observed in certain cases, leading us to omit the simulated end points for unstable solutions from our plots.

We encourage readers to explore these dynamics further by including the data points for the unstable r_{01} and r_{04} solutions in the plots. Additionally, slight modifications to the initial conditions in the `select_and_solve` function, available in the `common_utils.py` module, can provide deeper insights into the behavior of these unstable solutions.

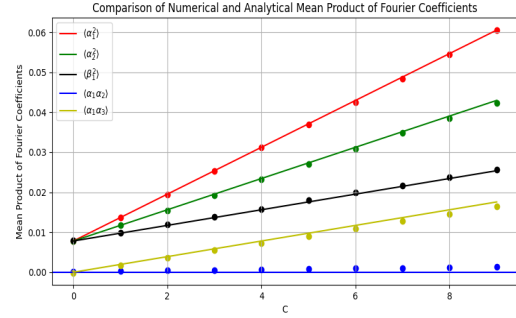
We invite readers to engage with the interactive simulation provided in the [Github repository](#) of the thesis. This tool offers a dynamic visualization of how the bifurcation diagrams evolve with changes in I_0 , providing an intuitive understanding of the system's behavior under varying external conditions.

3.3 Analysis of Fourier Statistics

In this section, we provide numerical support for the theoretical derivations discussed in Section 2.3. The following graphs compare theoretical predictions (represented by lines) with numerical simulations across different values of B , or C , respectively. The dots represent averages of 10,000 realizations of a quenched, Gaussian white noise process with variance V_θ .



(a) Parameters are $A = 1$, $C = 1$, and $N = 64$.



(b) Parameters $A = 1$, $B = 0$, and $N = 64$

Figure 4: Numerical experimental validations of theoretical predictions.

After verifying this, we examine the probability distributions previously discussed. Specifically, we focus on the first mode, as it is relevant for instability. We confirm that α_1 and β_1 are zero-mean, normally distributed with the calculated variances. Additionally, we check the distributions of the amplitudes and phases for the first mode.

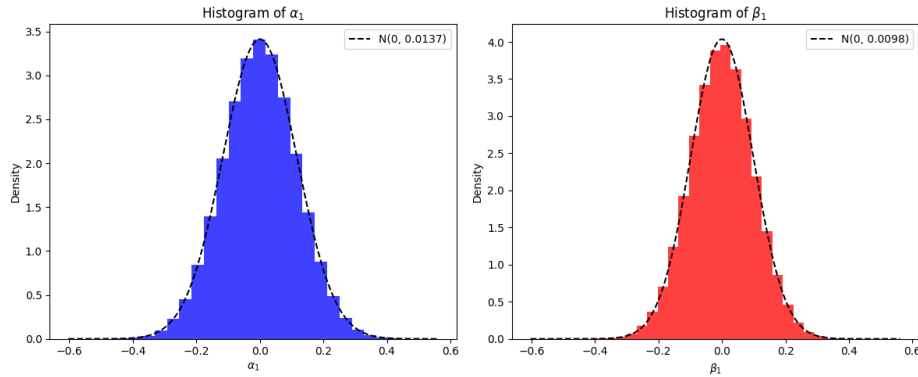


Figure 5: Histograms of α_1 and β_1 with overlaid normal distributions indicating expected variances.

We also check this for the distributions of R_j and ψ_j , as we derived in Section-2.3. Recall that we saw

$$R_j \sim \text{Rayleigh} \left(\sqrt{\langle \alpha_j^2 \rangle + \langle \beta_j^2 \rangle} \right),$$

$$\tan(\psi_j) = \frac{\beta_j}{\alpha_j} \sim \text{Cauchy} \left(0, \frac{\sqrt{\langle \beta_j^2 \rangle}}{\sqrt{\langle \alpha_j^2 \rangle}} \right),$$

which implies that

$$\psi_j = \arctan \left(\frac{\beta_j}{\alpha_j} \right) \sim \text{Uniform} \left(-\frac{\pi}{2}, \frac{\pi}{2} \right) \quad \text{if } \langle \alpha_j^2 \rangle = \langle \beta_j^2 \rangle.$$

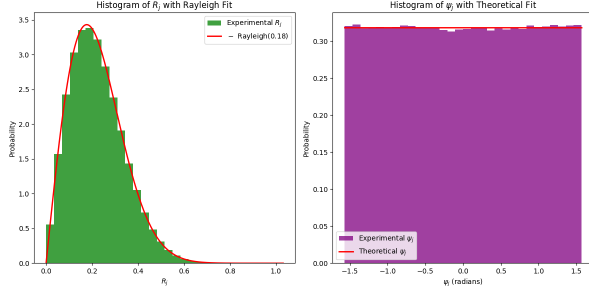


Figure 6: Distribution of R_1 and ψ_1 with $C = 0$.

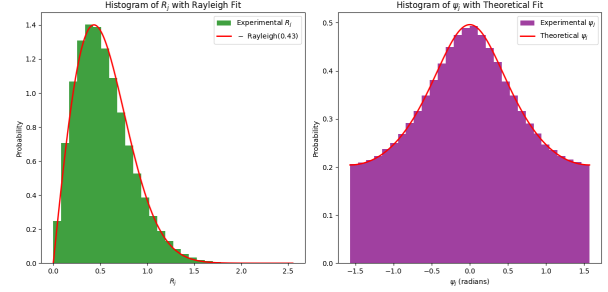


Figure 7: Distribution of R_1 and ψ_1 with $C = 10$.

In addition to verifying the analytical distributions, a key insight from this analysis is that increasing C makes it more likely for the phase of the first mode to be close to zero. Heuristically, neurons with smaller phases in the first mode are more likely to form bumps. Thus, as C increases, there will be more neurons with phases closer to zero, leading to less bias in the network and fewer chances to form hotspots.

Initially, we might hypothesize that we could monotonically decrease the variance, and in the limit of $C \rightarrow \infty$, the probability of sampling zero would be one, resulting in no hotspots in the network. However, this hypothesis turns out to be incorrect, as the variance plateaus as a function of C . Therefore, this reasoning is invalid according to this heuristic.

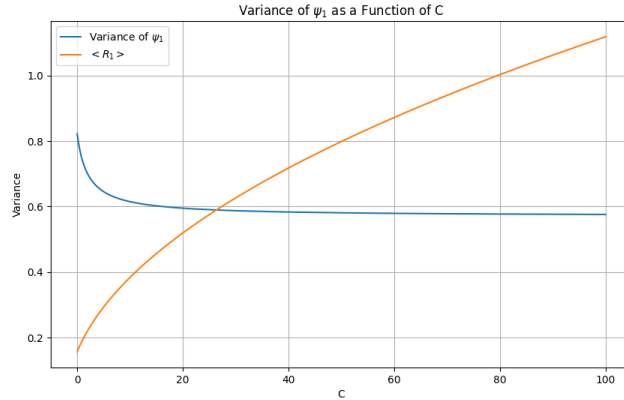


Figure 8: The variance of ψ_1 initially decreases but eventually plateaus.

3.4 Assessment of Spatial Stability

In this section, we provide numerical support for the theoretical derivations discussed in Section 2.2 and 2.4 regarding the spatial stability conditions. Remember that we had obtained for the case without quenched variability, the critical

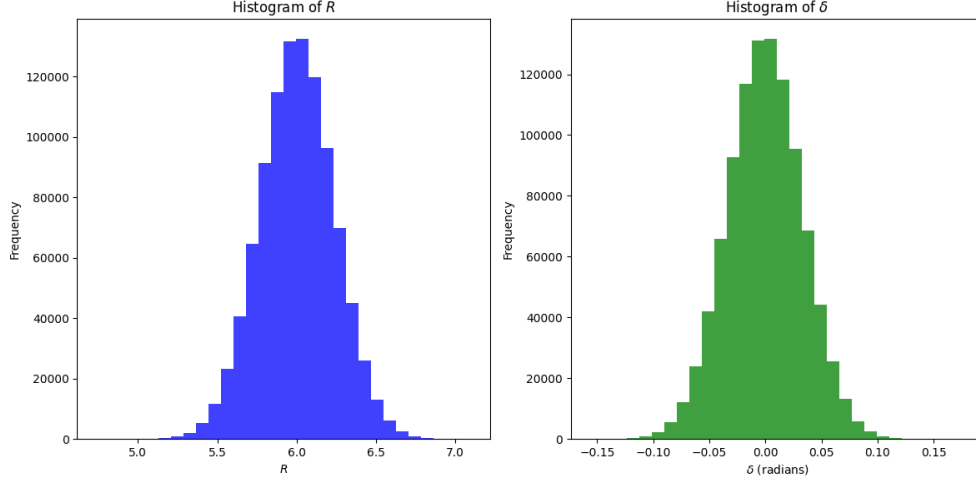


Figure 9: Histograms of R and δ showcasing their frequency distributions and demonstrating how the parameters R_1 and ϕ_1 influence the calculated values of R and δ in the system. $C=1$, $W_1 = 6$

value

$$W_1^{cr} = \frac{2}{\phi'_0}$$

and for the case with quenched variability,

$$W_1^{cr} = \frac{2}{\phi'_0} - \langle R_1 \rangle$$

where $\langle R_1 \rangle$ is the expected value of the first amplitude in the Fourier series.

For this experiment, we basically simulate the ring dynamics for different values of W_1 , and get the amplitude of the bump that is formed at the final timestep. Amplitude zero indicates no bump was formed.

We first observe for the deterministic case that the numerical experiments agree with the theoretical results. In particular, for values greater than the critical a Turing bifurcation happens, i.e. a bump forms.

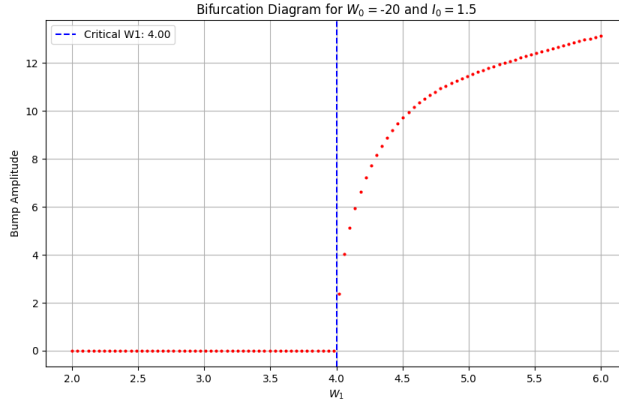


Figure 10: Bifurcation diagram for W_1 with $W_0 = -20$ and $I_0 = 1.5$.

We also observe that there is two kinds of bumps, one of greater amplitude and one smaller which is the one we try to look at in the picture, thus the motivation for choosing W_0 so small, in order to get only the small bump even for W_1 big. Note this is not that relevant for our purpose, as we take the amplitude interested in studying whether a bump forms or not, and not to see how big the amplitude is.

Including simulations with variability in our numerical experiments allows us to compare the two scenarios. This effect is illustrated in Figure 11. Specifically, we observe that memory recovery is possible for lower values of W_1 with variability, supporting the theoretical claim that variability enhances memory storage capacity.

Unlike the scenario without variability, each simulation with variability results in a different amplitude value. Consequently, I performed 20 iterations for each W_1 value, plotting their mean (blue dots) with a 95% confidence interval.

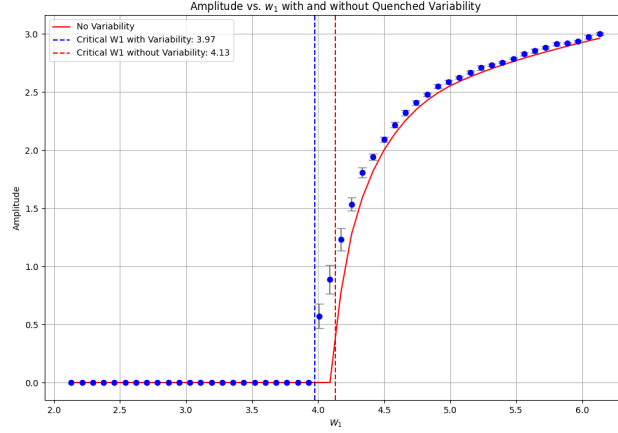


Figure 11: Bifurcation diagram for $A = 1, B = 0, C = 0$.

The amplitude for the variability case is calculated using the function in Listing 3. In this scenario, even though when no distinct bump is formed, the system reaches a noisy state resulting in a non-zero amplitude. However, for situations without a bump, we want this metric to be zero. Thus, I determined an appropriate threshold value by visual inspection. For amplitudes below this threshold, the amplitude is set to zero.

Finally, we inspect how increasing noise reduces the critical value of W_1 , both theoretically and in simulations. In particular, we observe that this occurs in a monotonic manner, demonstrating that increasing noise monotonically can enhance memory storage capacity.

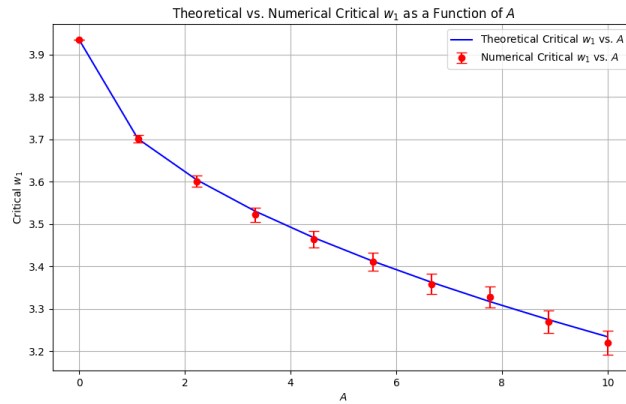


Figure 12: How increasing the noise lowers the critical value of W_1 .

For this section, we also include an interactive simulation where the reader can manipulate interactively the value of W_1 and see the changes in dynamics. The Jupyter notebook for running simulations, can be found [here](#).

3.5 On Hotspots

In the deterministic case, all bumps formed at phase zero. However, in the stochastic scenario, we observed different phase shifts. Despite starting with a spatial perturbation centered at phase zero, the center of the final activity profile shifted.

We investigated whether certain regions in the ring network, termed hotspots, were more likely to form bumps. Our hypothesis was that neurons with smaller phases ψ_1 and larger amplitudes R_1 were more likely to form bumps due to increased spatial perturbation from variability.

We tested this with 10,000 simulations, recording the phases of neurons with the three smallest ψ_1 and the phases where bumps formed. The results showed no clear correlation, indicating no causality. The same holds for the three largest R_1 . I conducted more experiments on this but did not reach any relevant conclusions. Therefore, I decided to leave this topic for future research, concluding that our heuristics might be incorrect.

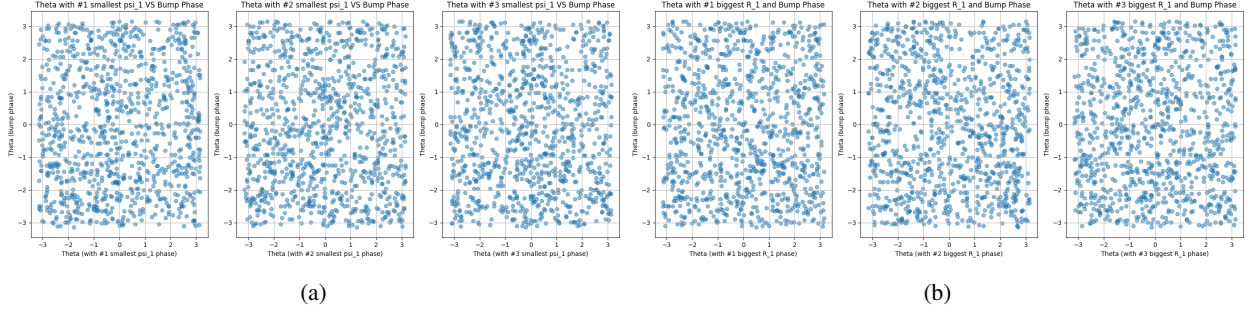


Figure 13: Phases of neurons with the three smallest ψ_1 and largest R_1 compared to bump phases.

4 Conclusion

In this thesis, we have explored the role of quenched variability in enhancing memory storage capacity within recurrent neural networks. Our theoretical analysis and numerical simulations demonstrate that variability in the connectivity can lower the critical threshold for memory recovery, effectively increasing the network's storage capacity. This result supports the hypothesis that incorporating variability into the system can be beneficial for memory encoding and retrieval processes.

We have also investigated the impact of noise on the formation of memory bumps and the presence of hotspots within the network. Our experiments show that increasing noise levels lead to a monotonic decrease in the critical value of W_1 , further confirming the capacity enhancement due to variability. However, our attempts to identify specific regions within the ring network that are more likely to form bumps, termed hotspots, did not yield any conclusive results. Despite extensive simulations, we found no clear correlation between the phases or amplitudes of neurons and the formation of bumps, suggesting that our initial heuristics may need revision.

Future research should focus on studying and understanding the existence of hotspots in these ring networks. Additionally, it is important to explore how these insights can enhance our understanding of brain dynamics. Since this variability arises from the interference of different environments, it suggests that there may be an optimal level of sparsity in environment encoding. Future work could involve developing analytical and numerical methods to determine this optimal level and identify the factors it depends on.

A Derivation of the Statistical Coefficients

We note that

$$\frac{1}{2\pi} \int_{-\pi}^{\pi} \langle \Delta W(\theta)^2 \rangle d\theta = \frac{1}{2\pi} \int_{-\pi}^{\pi} V(\theta) d\theta = A + \frac{C}{2} = \sum_{j=1}^N (\langle \alpha_j^2 \rangle + \langle \beta_j^2 \rangle), \quad (14)$$

where the second equality comes from integrating $V(\theta)$ as in 8, seeing that the terms with $\cos(\theta)$ and $\cos(2\theta)$ vanish if we integrate over a full period. The third equality comes from applying Parseval's Theorem, using the Fourier series expression 9.

We also see that

$$\frac{1}{\pi} \int_{-\pi}^{\pi} V(\theta) \cos \theta d\theta = B = 2 \sum_{j=1}^{N-1} (\langle \alpha_j \alpha_{j+1} \rangle + \langle \beta_j \beta_{j+1} \rangle), \quad (15)$$

where we derived the first integral using the two different expressions for $V(\theta)$, both as in 8 (first equality) and 10 (second equality).

In particular,

$$\frac{1}{\pi} \int_{-\pi}^{\pi} \left(A + \frac{C}{2} + B \cos(\theta) + \frac{C}{2} \cos(2\theta) \right) \cos(\theta) d\theta = B$$

since the other terms either vanish by integrating cosine over a full period or by the orthogonality argument between \cos and $\cos(2\theta)$.

For the second equality, given 10, we observe, using the product-to-sum identities,

$$\int_{-\pi}^{\pi} \cos((j-l)\theta) \cos(\theta) d\theta = \frac{1}{2} \left[\int_{-\pi}^{\pi} \cos((j-l+1)\theta) d\theta + \int_{-\pi}^{\pi} \cos((j-l-1)\theta) d\theta \right]$$

The integral of $\cos(k\theta)$ over $-\pi$ to π is zero unless $k = 0$, where it equals 2π . Thus, non-zero contributions occur when $j-l+1 = 0$ or $j-l-1 = 0$ (i.e., $j = l+1$ or $j = l-1$). The non-zero integral equates to 2π . Thus,

$$\frac{1}{\pi} \int_{-\pi}^{\pi} V(\theta) \cos(\theta) d\theta = \sum_{j=1}^{N-1} (\langle \alpha_j \alpha_{j+1} \rangle + \langle \beta_j \beta_{j+1} \rangle) + (\langle \alpha_{j+1} \alpha_j \rangle + \langle \beta_{j+1} \beta_j \rangle) = 2 \sum_{j=1}^{N-1} (\langle \alpha_j \alpha_{j+1} \rangle + \langle \beta_j \beta_{j+1} \rangle)$$

and the factor of 2 arises from a symmetry assumption.

Using a similar argument with 8 and 10, we also observe

$$\frac{1}{\pi} \int_{-\pi}^{\pi} V(\theta) \cos 2\theta d\theta = \frac{C}{2} = 2 \sum_{j=1}^{N-2} (\langle \alpha_j \alpha_{j+2} \rangle + \langle \beta_j \beta_{j+2} \rangle) + \langle \alpha_1^2 \rangle - \langle \beta_1^2 \rangle. \quad (16)$$

From 14, and assuming that the power is distributed evenly amongst all N terms on the right hand side, as is the case for a white noise process,

$$\langle \alpha_1^2 \rangle + \langle \beta_1^2 \rangle = \frac{1}{N} \left(A + \frac{C}{2} \right),$$

$$\langle \alpha_1^2 \rangle - \langle \beta_1^2 \rangle = \frac{C}{4N}.$$

where the second relation arises due to the spatial inhomogeneity of the quenched variability.

Using these two equations, we derive expressions for $\langle \alpha_1^2 \rangle$ and $\langle \beta_1^2 \rangle$ as follows:

$$\langle \alpha_1^2 \rangle = \frac{1}{2N} \left(A + \frac{3C}{4} \right),$$

$$\langle \beta_1^2 \rangle = \frac{1}{2N} \left(A + \frac{C}{4} \right).$$

It is important to note that this second relation due to the spatial inhomogeneity of the quenched variability is applicable only when $j = 1$. For other indices $j \neq 1$, the expressions simplify to:

$$\langle \alpha_j^2 \rangle = \langle \beta_j^2 \rangle = \frac{1}{2N} \left(A + \frac{C}{2} \right).$$

For the correlations between consecutive coefficients, which are crucial for understanding the dynamics across different terms of the series, we assume that the power is distributed evenly amongst all terms from 15. This assumption leads to

$$\langle \alpha_j \alpha_{j+1} \rangle = \langle \beta_j \beta_{j+1} \rangle = \frac{B}{4N}.$$

Similarly, using the same argument for Equation 16 demonstrates that

$$\langle \alpha_j \alpha_{j+2} \rangle = \langle \beta_j \beta_{j+2} \rangle = \frac{C}{8N},$$

highlighting the modulation effects not only for adjacent coefficients but also for those separated by one term.

B Derivation of the Distribution of R_j and ψ_j

Given that $R_j = 2\sqrt{\alpha_j^2 + \beta_j^2}$ and α_j and β_j are zero-mean Gaussian random variables with variances $\langle \alpha_j^2 \rangle$ and $\langle \beta_j^2 \rangle$ respectively, we analyze the distribution of R_j as follows.

The expression $\alpha_j^2 + \beta_j^2$ represents the squared norm of a vector composed of Gaussian components. If α_j and β_j are independent, then α_j^2 and β_j^2 are chi-squared distributed with 1 degree of freedom, scaled by their variances. Each component α_j^2 and β_j^2 can be described as scaled chi-squared variables

$$\begin{aligned}\alpha_j^2 &\sim \langle \alpha_j^2 \rangle \chi_1^2, \\ \beta_j^2 &\sim \langle \beta_j^2 \rangle \chi_1^2.\end{aligned}$$

The sum $\alpha_j^2 + \beta_j^2$ is then a chi-squared variable scaled by $\langle \alpha_j^2 \rangle + \langle \beta_j^2 \rangle$,

$$\alpha_j^2 + \beta_j^2 \sim (\langle \alpha_j^2 \rangle + \langle \beta_j^2 \rangle) \chi_1^2.$$

This is distributed according to a gamma distribution with 2 degrees of freedom. The square root of a chi-squared variable, $\sqrt{\alpha_j^2 + \beta_j^2}$, follows a Rayleigh distribution.

$$\sigma = \sqrt{\frac{\langle \alpha_j^2 \rangle + \langle \beta_j^2 \rangle}{2}}.$$

Since $R_j = 2\sqrt{\alpha_j^2 + \beta_j^2}$, the scaling factor of 2 modifies the Rayleigh distribution to

$$R_j \sim \text{Rayleigh} \left(2 \cdot \sqrt{\langle \alpha_j^2 \rangle + \langle \beta_j^2 \rangle} \right) = \text{Rayleigh} \left(2 \cdot \sqrt{\frac{A + \frac{C}{2}}{N}} \right) \quad \text{for all } j.$$

On the other side, we analyze the distribution of ψ_j under two cases.

If $\langle \alpha_j^2 \rangle = \langle \beta_j^2 \rangle$, then the ratio $\frac{\beta_j}{\alpha_j}$ follows a standard Cauchy distribution due to the identical scaling of the numerator and denominator by their Gaussian distributions

$$\frac{\beta_j}{\alpha_j} \sim \text{Cauchy}(0, 1).$$

The arctangent of a standard Cauchy distributed variable is uniformly distributed over the interval $[-\frac{\pi}{2}, \frac{\pi}{2}]$

$$\psi_j = \arctan \left(\frac{\beta_j}{\alpha_j} \right) \sim \text{Uniform} \left(-\frac{\pi}{2}, \frac{\pi}{2} \right) \quad \text{if } \langle \alpha_j^2 \rangle = \langle \beta_j^2 \rangle.$$

If $\langle \alpha_j^2 \rangle \neq \langle \beta_j^2 \rangle$, the ratio $\frac{\beta_j}{\alpha_j}$ follows a general Cauchy distribution with a scale parameter γ that depends on the variances:

$$\gamma = \frac{\sqrt{\langle \beta_j^2 \rangle}}{\sqrt{\langle \alpha_j^2 \rangle}},$$

and thus

$$\tan(\psi_j) = \frac{\beta_j}{\alpha_j} \sim \text{Cauchy} \left(0, \frac{\sqrt{\langle \beta_j^2 \rangle}}{\sqrt{\langle \alpha_j^2 \rangle}} \right) = \text{Cauchy} \left(0, \sqrt{\frac{A + \frac{C}{4}}{A + \frac{3C}{4}}} \right) \quad \text{if } \langle \alpha_j^2 \rangle \neq \langle \beta_j^2 \rangle.$$

C Derivation of Amplitude R and Phase Shift δ

We consider the expression involving the spatially modulated synaptic connectivity:

$$W(\theta) = W_0 + W_1 \cos(\theta) + R_1 \cos(\theta + \phi_1),$$

which can be simplified to a single cosine term. The expanded form of $R_1 \cos(\theta + \phi_1)$ is given by the trigonometric identity:

$$R_1 \cos(\theta + \phi_1) = R_1 (\cos(\theta) \cos(\phi_1) - \sin(\theta) \sin(\phi_1)).$$

Substituting into the original expression, we get:

$$W(\theta) = W_0 + (W_1 + R_1 \cos(\phi_1)) \cos(\theta) - R_1 \sin(\phi_1) \sin(\theta).$$

To combine these into a single cosine term, we rewrite it as:

$$W(\theta) = W_0 + A \cos(\theta) + B \sin(\theta),$$

where $A = W_1 + R_1 \cos(\phi_1)$ and $B = -R_1 \sin(\phi_1)$. This expression is equivalent to:

$$W(\theta) = W_0 + R \cos(\theta - \delta),$$

where R and δ are determined as follows:

$$R = \sqrt{A^2 + B^2} = \sqrt{(W_1 + R_1 \cos(\phi_1))^2 + (R_1 \sin(\phi_1))^2} = \sqrt{W_1^2 + 2W_1 R_1 \cos(\phi_1) + R_1^2},$$

$$\tan(\delta) = \frac{B}{A} = \frac{-R_1 \sin(\phi_1)}{W_1 + R_1 \cos(\phi_1)}.$$

Thus, δ is computed by:

$$\delta = \arctan\left(\frac{-R_1 \sin(\phi_1)}{W_1 + R_1 \cos(\phi_1)}\right).$$

D Supplementary Code

Listing 1: Code to Filter Theoretically Derived Solutions Using a Tolerance Mask

```
def apply_mask(w0, I_0, r_func, tolerance=1e-4):
    r_values = r_func(w0, I_0)
    mask = np.isclose(r_values, nonlinearity(w0 * r_values + I_0), atol=tolerance)

    r_values_filtered = np.where(mask, r_values, np.nan)
    w0_filtered = np.where(mask, w0, np.nan)

    return w0_filtered, r_values_filtered
```

Listing 2: Code to Simulate from Selected Initial Conditions and Evaluate their Stability.

```
def select_and_solve(w0, r_filtered, I_0, func):
    non_nan_indices = ~np.isnan(r_filtered)
    w0_non_nan = w0[non_nan_indices]

    if len(w0_non_nan) == 0:
        return np.array([]), np.array([])

    indices_selected = np.linspace(0, len(w0_non_nan) - 1, min(len(w0_non_nan), 10), dtype=int)
    w0_selected = w0_non_nan[indices_selected]
    r_num = []
    t_span = [0, 100]
    t_eval = np.linspace(t_span[0], t_span[1], 2000)

    for w0_val in w0_selected:
        r0 = [func(w0_val, I_0)] # HERE: check stability by adding 0.01
        sol = solve_ivp(dr_dt, t_span, r0, args=(w0_val, I_0), t_eval=t_eval, method='RK45')
        r_num.append(sol.y[0, -1])

    return w0_selected, r_num
```

Listing 3: Code to Get the Amplitude of the First Fourier Mode of the Final Activity Profile

```
def calculate_bump_amplitude(self, threshold = 0.2, filter_noise = False):

    final_state = self.dynamics.y[:, -1]

    fft_result = np.fft.fft(final_state)

    first_mode_amplitude = np.abs(fft_result[1])

    if filter_noise and first_mode_amplitude < threshold:
        return 0

    return first_mode_amplitude
```

The GitHub repository for this thesis, which includes all Python scripts for generating graphs and relevant Jupyter notebooks for running simulations, can be found [here](#).

References

- [1] Aaron Milstein, Yan Li, Katie Bittner, Christine Grienberger, Ivan Soltesz, Jeffrey Magee, et al. Bidirectional synaptic plasticity rapidly modifies hippocampal representations. *eLife*, 10:e73046, 2021. doi: 10.7554/eLife.73046.
- [2] Katie Bittner, Aaron Milstein, Christine Grienberger, Sandro Romani, and Jeffrey Magee. Behavioral time scale synaptic plasticity underlies ca1 place fields. *Science*, 357:1033–1036, 2017. doi: 10.1126/science.aan3846.
- [3] PY Li and Alex Roxin. Rapid memory encoding in a recurrent network model with behavioral time scale synaptic plasticity. *PLOS Computational Biology*, 19(8):e1011139, 2023. doi: 10.1371/journal.pcbi.1011139. URL <https://doi.org/10.1371/journal.pcbi.1011139>.
- [4] Alfio Quarteroni and Fausto Saleri. *Scientific Computing with MATLAB and Octave*. Springer, 2 edition, 2006.